Title

Iron-crosslinked Rososome with robust stability and high drug loading for synergistic cancer therapy

Authors

Xue, Xiangdong

Ricci, Marina

Qu, Haijing

et al.

Publication Date

2021

DOI

10.1016/j.jconrel.2020.10.013

Peer reviewed

HHS Public Access

Author manuscript

J Control Release. Author manuscript; available in PMC 2022 January 10.

Published in final edited form as:

J Control Release. 2021 January 10; 329: 794–804. doi:10.1016/j.jconrel.2020.10.013.

Iron-Crosslinked Rososome with Robust Stability and High Drug Loading for Synergistic Cancer Therapy

Xiangdong Xue[a,1], **Marina Ricci**[a,b,1], **Haijing Qu**[a], **Aaron Lindstrom**[a], **Dalin Zhang**[a], **Hao Wu**[a], **Tzu-Yin Lin**[c], **Yuanpei Li**[a]

[a]Department of Biochemistry and Molecular Medicine, UC Davis Comprehensive Cancer Center, University of California Davis, Sacramento, CA 95817, USA.

[b]Department of Clinical and Biological Sciences, University of Torino, Corso Raffaello 30, Turin, 10125, Italy.

[c]Division of Hematology/Oncology, Department of Internal Medicine, University of California Davis, Sacramento, CA 95817, USA.

Abstract

Development of liposomal nanomedicine with robust stability, high drug loading and synergistic efficacy is a promising strategy for effective cancer therapy. Here, we present an iron-crosslinked rosmarinic liposome (Rososome) which can load high contents of drugs (including 25.8% rosmarinic acid and 9.04% doxorubicin), keep stable in a high concentration of anionic detergent and exhibit synergistic anti-cancer efficacy. The Rososomes were constructed by rosmarinic acid-lipid conjugates which not only work synergistically with doxorubicin by producing reactive oxygen species but also provide catechol moieties for the iron cross-linkages. The cross-linkages can lock the payloads tightly, endowing the crosslinked Rososome with better stability and pharmacokinetics than its non-crosslinked counterpart. On the syngeneic mouse model of breast cancer, the iron-crosslinked Rososomes exhibit better anticancer efficacy than free rosmarinic acid, doxorubicin, non-crosslinked Rososome and commercial liposomal formulation of doxorubicin (DOXIL). This study introduces a novel strategy for the development of liposomes with robust stability, high drug loading and synergistic anti-cancer efficacy.

Corresponding author: Yuanpei Li; lypli@ucdavis.edu.

CRediT authorship contribution statement

Xiangdong Xue: Conceptualization, Methodology, Investigation, Formal analysis, Validation, Writing - original draft, Writing - review & editing. **Marina Ricci:** Methodology, Investigation, Formal analysis, Validation, Writing - review & editing. **Haijing Qu**: Investigation. **Aaron Lindstrom**: Writing - review & editing. **Dalin Zhang:** Resources. **Hao Wu:** Resources. **Tzu-yin Lin:** Methodology. **Yuanpei Li:** Supervision, Validation, Project administration, Writing - review & editing.

[1]X. Xue and M. Ricci contributed equally.

Competing interests

The authors declare no competing financial interest.

Keywords

chemotherapy; liposome; synergistic effect; crosslink; drug delivery

1. Introduction

Chemotherapy employs cytotoxic agents for cancer treatment and has been widely utilized in the clinic.[1, 2] Despite the clinical effectiveness of slowing down cancer development, chemotherapy inevitably induces severe side effects, due to its non-selective damages to both cancerous and normal cells.[3, 4] Moreover, single model chemotherapy only contributes to marginal anticancer efficacy, if the cancers are highly malignant or drug-resistant. A combination of chemotherapy with other therapeutic modalities may trigger a synergistic effect which leads to better outcomes than the single model therapy.[5–7] However, simply co-administration of multiple drugs may compromise the synergistic effect, due to the disparities in terms of pharmacokinetics, biodistribution and tissue uptake. Nanomedicine sheds new light on the cancer chemotherapy by virtue of its myriad advantages in the field of drug delivery.[8–11] Unlike conventional chemotherapy, nanomedicines selectively deliver the chemotherapeutics to the solid tumor by taking advantage of enhanced permeability and retention (EPR) effect [12] or transcytosis through tumor endothelial cells[13], thus extensively alleviate the side effects and improve the efficacy. Moreover, multiple drugs can be concomitantly loaded in one single nanoparticle, so that their disparities in pharmacokinetics, biodistributions and tissue uptake can be unified.

Excessive reactive oxygen species (ROS) disequilibrate the cellular redox homeostasis to damage the DNA and cell membranes, and consequently cause cell apoptosis.[14–16] It has been reported that cytotoxic ROS works together with chemotherapy and exhibits excellent synergistic efficacy.[17–19] ROS can be produced either by photosensitizer[20–23] or molecular drugs[24–28]. The photosensitizer absorbs light power to drive the ROS production, e.g. photodynamic therapy.[29, 30] However, the limited tissue penetration of light hinders the application of photodynamic therapy. Comparatively, molecular drugs don’t need extracorporeal stimulation for ROS generation, making them more feasible for in vivo applications. Intracellular redox homeostasis, such as high glutathione (GSH) level in the cytoplasm, can rapidly scavenge ROS to ameliorate the cell apoptosis.[31, 32] Therefore, the intracellular ROS production needs to be excessive to the GSH level to realize the cell-killing effect. In other words, the treating concentration of molecular drugs should be sufficient enough to induce cytotoxicity. However, the drug loading capacities of the commonly used nanocarriers, such as liposomes, micelles and polymeric nanoparticles, are generally not exceeding 15%.[33–35] The low loading capacity makes conventional nanocarrier incompetent to deliver high content of molecular drugs and chemotherapeutics concomitantly. To achieve a synergistic effect between chemotherapy and ROS-therapy, nanomedicine with a high loading capacity of ROS-producer are desirable to be developed.

Liposome is one of the most successful nanomedicines for drug delivery, plenty of liposomal formulations of chemotherapeutic drugs were listed in the market, such as DOXIL,

Lipoplatin, Myocet and Depocyt, etc. Although promising, conventional liposomes still suffer from some shortcomings. The liposomal structure is constructed by amphiphilic lipids which self-assembled by the force of hydrophobic interaction. This weak interaction may not constrain the payloads tightly in the liposome, and thereby, lead to poor stability and drug leak. Moreover, the drug loading of the conventional liposomes is generally low, due to the presence of a large proportion of lipid carrier. The poor stability and undesirable drug loading make the conventional liposomes exhibit unsatisfactory efficacy. Rosmarinic acid (RA) is a metabolite found in plants such as rosemary and salvia.[36, 37] RA not only shows excellent antimicrobial, anti-viral activities, but also induces cell death or apoptosis by elevating intracellular ROS level.[38, 39] Another key thing is, RA contains an active carboxylic acid (Figure S1) which can react with the building blocks and make RA become part of the nanocarrier, and therefore, largely improve the drug loading. To this end, RA was covalently conjugated to an amphiphilic lipid (1-palmitoyl-2-hydroxy-sn-glycero-3-phosphocholine) by reacting with the hydroxyl group and yielded a rosmarinic-lipid (Figure S1). As shown in Scheme 1, the amphiphilic rosmarinic-lipids can readily co-assemble with DSPE-mPEG$_{2000}$ (1,2-distearoyl-sn-glycero-3-phosphoethanolamine with conjugated methoxyl polyethylene glycol) and soy PC (L-α-phosphatidylcholine) to form rosmarinic liposome (termed as Rososome). Rososome was composed of rosmarinic-lipids which contained equivalent amounts of RA and lipid. This particular chemical composition makes the RA content in Rososome reach 25.8% (precluded DSPE-mPEG$_{2000}$ and PC). Such high drug loading guarantees the ROS-producing power of Rososome. As a kind of liposome, Rososome is supposed to have a high potential for the encapsulation of hydrophilic drugs. To combine ROS-therapy with chemotherapy in Rososome, hydrophilic doxorubicin hydrochloride (DOX) was encapsulated to form Rososome@DOX (R@DOX). Similar to the liposome, Rososome may also face the obstacles of low stability which can lead to drug leak and undesirable pharmacokinetics. We found that RA has two catechol moieties that can coordinate with ferric iron[40–43] and form iron-catechol crosslinkages to bridge the rosmarinic-lipids. These crosslinkages can tightly constrain the liposomal structure and form crosslinked R@DOX (X-R@DOX). The crosslinking strategy was supposed to render the Rososomes with robust stability which is beneficial to pharmacokinetics and *in vivo* performance. Once the Rososome delivered DOX into cancer cells, RA can produce ROS and work with DOX synergistically to achieve better anticancer efficacy.

2. Materials and methods

2.1. Materials and instruments

Rosmarinic acid, dicyclohexylcarbodiimide (DCC), 4-dimethylaminopyridine (DMAP), organic solvents, such as chloroform, dichloromethane, acetic acid and methanol, were purchased from Sigma-Aldrich Inc (MO, USA). 1-palmitoyl-2-hydroxy-sn-glycero-3-phosphocholine and phosphatidylcholine (PC) were bought from Avanti Polar Lipids Inc (AL, USA). 1,2-distearoyl-sn-glycero-3-phosphoethanolamine with conjugated methoxyl poly (ethylene glycol) (DSPE-mPEG$_{2000}$) was bought from Laysan Bio Inc (AL, USA). DOXIL was purchased from Janssen Pharmaceutica (NV, USA). LysoTracker Deep Red and Hoechst 33342 were purchased from Thermo Fisher Scientific Inc (MA, USA). The rosmarinic-lipids were characterized by matrix-assisted laser desorption/ionization-time of

flight mass spectrometry (Bruker UltraFlextreme) and nuclear magnetic resonance spectrometer (600 MHz Bruker Avance III). The cell uptake, ROS production and apoptosis were carried on by 20-color flow cytometry (Fortessa, BD). The cellular distribution was conducted by a confocal laser scanning microscope (LSM810, Carl Zeiss). The animal imaging studies were investigated by ChemiDoc Imaging Systems (ChemiDoc XRS+, Bio-Rad). The UV-vis absorption of doxorubicin was measured by a UV-vis spectrometer (UV-1800, Shimadzu) and the fluorescence was tested by a fluorophotometer (RF-6000, Shimadzu).

2.2. Synthesis and purification of rosmarinic-lipid

288 mg rosmarinic acid (0.8 mmol), 328 mg dicyclohexylcarbodiimide (DCC, 1.6 mmol) and 48 mg 4-Dimethylaminopyridine (DMAP, 0.4 mmol) were dissolved in 100 mL chloroform and vigorously stirred in an ice bath for 30 min. Then, 200 mg lipid (1-palmitoyl-2-hydroxy-sn-glycero-3-phosphocholine, 0.4 mmol) was added to the reaction system and stirred for another 48 h in ambient temperature. The reaction system was filtered to remove the sediments, then applied to column chromatography with eluents of a dichloromethane/methanol/acetic acid/water mixture (60:30:8:2, volume ratio). The resultant rosmarinic-lipid was characterized by matrix-assisted laser desorption/ionization time-of-flight (MALDI-TOF) mass spectrometry and nuclear magnetic resonance (NMR).

2.3. Preparation of the Rososomes

The Rososomes were prepared by the classic film hydration method. 6 mg rosmarinic-lipid, 3 mg phosphatidylcholine (PC) and 1 mg 1,2-distearoyl-sn-glycero-3-phosphoethanolamine with conjugated methoxyl poly (ethylene glycol) (DSPE-mPEG$_{2000}$) were dissolved in chloroform/methanol mixture (3:1, volume ration) in a round bottom flask. The solvent was evaporated to allow lipids to form a film in the flask. Then, PBS or doxorubicin PBS solution (1 mg) was added to rehydrate the film followed by 3 min sonication to yield Rososome or Rososome@DOX (R@DOX).

2.4/ Fabrication of cross-linked Rososomes

The cross-linked Rososomes followed the same procedure that we made Rososome and R@DOX. Briefly, 6 mg rosmarinic-lipid, 3 mg PC and 1 mg DSPE-mPEG$_{2000}$ were dissolved in chloroform/methanol mixture (3:1, v/v) in a round bottom flask, then 1 mg $FeCl_3 6H_2O$ was added into the solution followed with 60 min incubation. After that, the same procedure of the film hydration method was applied to form cross-linked Rososome and Rososome@DOX (X-R@DOX).

2.5. Characterization of Rososomes.

The size distribution and polydispersity index (PDI) of Rososomes were measured by dynamic light scattering (ZS-nano, Malvern, UK). Their morphology was observed by transmission electron microscopy (TEM, Talos L120C, FEI) with 80 kV acceleration voltage.

2.6. Encapsulation efficiency measurements

2 mg/mL R@DOX or X-R@DOX were loaded in a centrifugal dialysis tube (MWCO is 7,000 Da) and applied to centrifugation (5000 rpm for 6 min). The unloaded DOX was spun down to the bottom tube and collected for UV-vis analysis. The concentrations of the unloaded DOX was quantified by a standard curve of DOX based on UV-vis absorbance. The encapsulation efficiency (EE%) of DOX was calculated by following the formula: EE% = [(Drug added - Free “unloaded drug”)/Drug added] *100. The drug loading (DL%) of DOX in Rososomes are calculated by DL% = [(Drug added - Free “unloaded drug”) / (Drug added + carrier)] *100. By calculation, the EE% of R@DOX is 98.7% and X-R@DOX is 99.3%. The DL% of R@DOX is 8.98% and X-R@DOX is 9.04%.

2.7. Investigation of the stability braced by iron (III) crosslinkers

2 mg/mL R@DOX and X-R@DOX were respectively incubated with or without 2 mM detergent (sodium dodecyl sulfate, SDS) for 12 h under room temperature. Then, the Rososomes were tested by dynamic light scattering. The changes in size distribution and polydispersity index were employed to demonstrate the advantages of crosslinkers in Rososomes.

2.8. Drug releasing pattern of Rososomes

DOX-loaded Rososomes, including R@DOX and X-R@DOX, were prepared to determine the drug-releasing profile. Aliquots of R@DOX or X-R@DOX were loaded in a dialysis tube with a 3,500 Da MWCO. The Rososomes were dialyzed against PBS buffer (pH 7.4) or acetate buffer (pH 5.0) at room temperature. The concentration of DOX remaining in the dialysis tube at different time points was measured by the fluorescence spectrometer. The concentrations of DOX was calculated by a fluorescence-based standard curve. Values were reported as the means for each duplicate sample.

2.9. Hemolysis test of Rososomes

Fresh blood was donated by healthy volunteers. First, 1 mL blood was diluted with 9 mL of PBS. The red blood cells (RBCs) were obtained by centrifugation of the blood suspension at 1000 g for 10 min. The RBCs were washed with 10 mL of PBS for 3 times and resuspended in 10 mL PBS for further use. 100 μL of diluted RBC was treated with R@DOX or X-R@DOX at different concentrations (1, 10, 100, 1000 μg/mL) by gently vortex and incubated at 37 °C for 4 h. The RBCs were centrifuged at 1000 g for 5 min, and 100 μL of the supernatant was transferred to a 96-well plate. Free hemoglobin in the supernatant was measured by the absorbance at 540 nm using a microplate reader (SpectraMax M2, Molecular Devices, USA). RBCs incubation with detergent (Triton-X 100) as a positive control and isosmotic solution (PBS) as a negative control. The percentage of hemolysis was calculated with the formula: RBCs hemolysis = $(OD_{sample} - OD_{negative\ control}) / (OD_{positive\ control} - OD_{negative\ control}) \times 100\%$. All the samples were run in triplicates.

2.10. Stability of the X-R@DOX in serum

R@DOX or X-R@DOX was incubated with 10% fetal bovine serum (FBS) at room temperature. The size distribution and polydisperse index were continuously monitored by dynamic light scattering in different days. All the samples were run in triplicates.

2.11. Cell culture

4T1 mouse breast cancer cells were seeded in tissue culture dishes with DMEM/F-12 medium supplemented with 10 μg/mL insulin. All cell cultural medium was supplemented with 10% FBS and 1% penicillin and streptomycin.

2.12. Cell viability analysis

4T1 cells were seeded in a 96-well plate for 24 h until they are fully attached. The cells were treated with Rososomes and the control materials, including free rosmarinic acid (RA), free doxorubicin (DOX), an FDA-approved liposomal formulation of doxorubicin (DOXIL®) and Rososomes (Rososomes, X-Rososome, R@DOX and X-R@DOX). Untreated 4T1 cells were used as control. The MTT assay was performed at a series of concentrations, including 0.1, 0.5, 1, 5, 10 and 50 μM, based on the molar concentrations of DOX.

2.13. Cell uptake evaluated by flow cytometry

Since DOX shows intrinsic fluorescence, the cell uptake of Rososomes was quantified by flow cytometry. The materials contained DOX, such as DOX, DOXIL, R@DOX and X-R@DOX were incubated with 4T1 cells for 24 h and collected for flow cytometry (BD FACSCanto) analysis. The concentration of all materials was calculated according to the equivalent concentration of DOX (1 μM).

2.14. Cell distribution measured by confocal laser scanning microscopy

4T1 cells were seeded in a glass-bottom Petri dish for 24 h until the cells were fully attached. The cells were treated with the materials contained 1 μM DOX, including DOX, DOXIL, R@DOX or X-R@DOX, for 24 hours. The PBS-treated cells were set as a negative control. Lysosomes were stained with a commercial LysoTracker Deep Red and the nucleus was stained by Hoechst 33342. The treated cells were washed twice with PBS and observed under a confocal laser scanning microscope (Zeiss LSM 800). For DOX observation, FITC channel was used; Cy5 channel was employed for observation of lysosomes. DAPI channel was for Hoechst 33342.

2.15. Pharmacokinetics Study

9 mice (FVB, female 6-week old) were randomly assigned to 3 groups (n=3). 8 mg/kg of DOX, R@DOX or X-R@DOX was i.v. administrated to the mice in these groups, respectively. The blood was collected at different times from the tail vein. 10 μL blood was collected each time and dissolved in 90 μL DMSO. The concentrations of DOX were quantified by a fluorescence spectrometer based on a standard curve of DOX. All animal experiments were strictly in compliance with the guidelines of Animal Use and Care Administrative Advisory Committee of the University of California, Davis.

2.16. Biodistributions of Rososomes

The biodistribution of Rososomes was evaluated by near-infrared fluorescence imaging (NIRFI) on 4T1 tumor-bearing mice. DOX is not suitable for *in vivo* imaging due to the limited penetration of its short-wavelength fluorescence. To facilitate the biodistribution imaging, the DOX in Rososomes was replaced by a hydrophilic near-infrared dye, indocyanine green (ICG), as a surrogate. 10 mg Rososomes or X-Rososomes encapsulated 0.5 mg ICG to form the Rososomes with near-infrared fluorescence (R@ICG or X-R@ICG) Then, 2 mg/kg R@ICG or X-R@ICG were i.v. injected into 4T1 tumor-bearing mice. The fluorescence of ICG was monitored at different time points. The mice were sacrificed at 72 h of *in vivo* imaging, their organs were collected for *ex vivo* imaging. The Rososomes distributed in the heart, liver, spleen, lung, kidney, intestine, muscle and tumor were indicated by ICG.

2.17. In vivo efficacy of Rososomes on orthotopic 4T1 breast cancer-bearing mice

To establish orthotopic 4T1 breast cancer-bearing mice, 1×10^5 4T1 cells were inoculated to the mammary fat pad of the BALB/c mice (female, 8-week old). Once the tumors reached the volume of 100 to 125 mm^3, the mice were randomly distributed into 8 groups (n=6) for the treatments. 8 mg/kg of the Rososomes and their controls, including PBS, RA, DOX, DOXIL, Rososome, X-Rososome, R@DOX or X-R@DOX were i.v. injected into 4T1 tumor-bearing mice every 3 days for two consecutive weeks. The dose of the administrated materials was calculated based on the equivalent concentration of DOX. The tumor volumes and body weight were monitored every 3 days. The organs of the mice (lung, liver, spleen, kidney and heart) were collected for histopathologic analysis.

2.18. Statistical analysis

Data statistics were analyzed by calculating the *t-test* between two groups, and one-way ANOVA analysis of variations for multiple groups. Unless otherwise noted, all results were expressed as the mean ± SD. A value of $p<0.05$ was considered statistically significant.

3. Results and discussion

3.1. Synthesis of Rosmarinic-lipid

Rosmarinic-lipid was synthesized by directly conjugating a rosmarinic acid with an amphiphilic lipid through esterification (Figure S1). The spectrum of mass spectrometry showed that the main M+[H]+ peak of *m/z* at 838.4 Da matched the theoretical mass (837.4 Da) of rosmarinic-lipid (Figure S2). The nuclear magnetic resonance (NMR) also fit the chemical-shift of the rosmarinic-lipid (Figure S3). Both spectra of MS and NMR supported that the rosmarinic-lipid was successfully synthesized. The purity of the resultant rosmarinic-lipid was characterized by thin-layer chromatography (TLC). As shown in Figure S4a, the rosmarinic-lipid displayed a single dot with different retention factor (Rf) comparing to the reactants (lipid and rosmarinic acid), indicating that the rosmarinic-lipid was successfully purified with high purity. The ester bond that attached rosmarinic acid and lipid is supposed to be very stable at neutral pH. Hence, we incubated rosmarinic-lipid with water at room temperature for 3 days and applied to TLC analysis. In parallel with fresh-

made rosmarinic-lipid, they both displayed a single dot with the same Rf on the TLC plate and showed no print at the Rf of RA (Figure S4b), demonstrating that the rosmarinic-lipid didn't suffer from spontaneous reduction.

3.2. Characterization of Rososomes

The rosmarinic-lipid can co-assemble with DSPE-mPEG$_{2000}$ and PC to form Rososome. As shown in Figure S5, Rososome exhibited liposomal structure with a broader and darker bilayer ring. The hydrodynamic diameter of Rososome was measured as 198.9 nm by dynamic light scattering (DLS) with a polydispersity index (PDI) of 0.194. To stabilize the liposomal structure, we added ferric iron to crosslink the Rososome. The iron-catechol coordination can bridge the rosmarinic lipids to form crosslinked Rososome (X-Rososome). X-Rososome showed a hydrodynamic diameter of 134.8 nm with a PDI of 0.139. The morphology of X-Rososome was similar to the Rososome, except that the bilayer ring became even thicker, which can be ascribed to the presence of iron-catechol crosslinkages (Figure S6). The size of X-Rososome is relatively smaller than Rososome, we speculated that the iron crosslinkages may compress the nanostructure. Rososomes harbor water affinity core which can encapsulate hydrophilic drugs as liposome does. Therefore, we loaded DOX into Rososome and X-Rososome to form Rososome@DOX (R@DOX) and X-Rososome@DOX (X-R@DOX), respectively. Figure 1a showed that the hydrodynamic diameter of R@DOX was 186.6 nm with a PDI of 0.136, indicating the R@DOX was homogeneous. The morphology of R@DOX was liposomal structure with a broader bilayer which can be observed without negative stain (Figure 1b). In comparison, X-R@DOX didn't show big changes in terms of size (180.1 nm) and PDI (0.156), but the bilayer ring became thicker and darker (Figure 1c and 1d), which may also be attributed to the iron-catechol crosslinkages. Such structural change is consistent with what is observed on Rososome and X-Rososome. After loading the DOX, the size of X-R@DOX became much larger than X-Rososome. We posit that the encapsulated DOX occupies the space in the core of X-Rososomes, and makes the size larger than the empty X-Rososomes. We also tested the surface charge of Rososomes before and after iron crosslink. The DOX-loaded Rososomes (R@DOX) showed a slightly negative charge (−5.86 mV) due to their PEG surface (Figure S7). After crosslinked by iron, the surface charge of Rososome (X-R@DOX) slightly changed to −2.88 mV (Figure S8). The slight changes upon the iron addition demonstrated that the iron crosslinkages didn't obviously alter the surface charge of Rososome.

3.3. Superior stabilities of iron crosslinked Rososomes

Crosslinking strategy is supposed to render Rososomes with robust stability, as these intricate iron-catechol bridges tightly constrain the liposomal structure. To validate the benefits of iron-catechol crosslinkages to the Rososomes, we incubated R@DOX or X-R@DOX with sodium dodecyl sulfate (SDS, an anionic detergent that can readily break down liposome) and monitored the changes in size and PDI. After incubation with SDS, the R@DOX changed from a single size distribution of 186.6 nm to two peaks (54 nm and 284 nm) and the PDI increased from 0.136 to 0.623 (Figure 1e), indicating that R@DOX can be easily broken down by SDS. In contrast, X-R@DOX remained the same size distribution around 180 nm. The PDI only exhibited a slight increase from 0.156 to 0.234 (Figure 1f). The stability studies with SDS demonstrated that the crosslinking strategy can profoundly

improve the stability of Rososomes, which would bring benefits to pharmacokinetics and *in vivo* efficacy. The time-dependent stability of R@DOX and X-R@DOX were also investigated in the presence of serum. The non-crosslinked R@DOX gradually increase the size from 200 nm to 330 nm while the PDI fluctuated within a narrow range (Figure S9), demonstrating that R@DOX was not stable and the liposomal structure tended to grow big in serum. The size and PDI of X-R@DOX fluctuated within a reasonable range (190~200 nm) for at least 10 days (Figure 1g). Comparatively, the iron-catechol crosslinking strategy can profoundly improve the stability of the Rososome.

3.4. Drug releasing behaviors of Rososomes

For controllable drug delivery, ideal nanomedicines are designed as stable nanostructure in the physiological conditions, and responsively release the drug at targeting locale by certain stimuli. Our Rososome has been proved with robust stability in the physiological condition (e.g. in serum). Then, we investigated whether the Rososomes are controllable for DOX release (Figure 1h). In physiological pH (7.4), R@DOX and X-R@DOX both released a little amount of DOX at the first few hours. After that, the R@DOX continuously released more doxorubicin. In comparison, the X-R@DOX reached a plateau and could prevent doxorubicin from being further releasing, demonstrating that our crosslinking strategy is an efficient way to improve the drug delivery capability of the lipososmes. Considering that metal chelation can be broken down by acidic pH,[44–46] R@DOX and X-R@DOX were respectively incubated in acetate buffer (pH 5.0) to monitor the pH-responsive drug-releasing profile. As shown in Figure 1h, R@DOX and X-R@DOX both exhibited burst releasing patterns in the first few hours, then reached a plateau. In comparison, R@DOX released more drugs (~80%) than X-R@DOX did (~70%). The releasing patterns demonstrated that the Rososomes were stable in the physiological condition but can responsively release the payloads by a specific stimulation, such as acidic pH.

3.5. Hemolysis of Rososomes

To evaluate the safety in the biosystem, we also tested the hemolysis of R@DOX and X-R@DOX (Figure 1i and Figure S10). Both Rososomes showed imperceptible hemolysis at different concentrations, compared to an isosmotic solution (PBS) and nonionic surfactant (Triton X-100). The hemolysis results indicated that Rososomes are suitable for biological use.

3.6. ROS producing capability of Rososomes

RA can boost the oxidative stress in cells by producing ROS which may work synergistically with DOX for better anti-cancer efficacy. Hence, we evaluated the ROS production in breast cancer cells (4T1) by treating with different RA-related formulations, including free RA, Rososome and X-Rososome. The PBS-treated cells were employed as a control. DCF-DA was employed to indicate the ROS production in cells. As shown in the flow cytometry results (Figure 2a), RA, Rososome and X-Rososome all can produce abundant ROS which was much higher than PBS control did.

3.7. Cell viability and synergistic efficacy of Rososomes

The high ROS production may exhibit a synergistic effect when combining with DOX. To evaluate the synergistic effect, we conducted cell viability experiments on 4T1 cells. The cells were incubated with different formulations, including free RA, free DOX, nanoformulation of RA (Rososome and X-Rososome), nanoformulation of DOX (DOXIL) and nanoformulation of RA/DOX combos (R@DOX and X-R@DOX). As shown in Figure 2b, the RA contained formulations, including free RA, Rososome and X-Rososome, exhibited some extent of anti-cancer efficacy which can be attributed to high oxidative stress caused by ROS. DOXIL, a liposomal formulation of DOX showed a modest therapeutic effect on 4T1 cells. In contrast, free DOX, R@DOX and X-R@DOX showed better efficacy compared to DOXIL. Free DOX was very effective *in vitro* because it can enter the cell nuclear directly without experiencing the drug-releasing process.[47] The R@DOX and X-R@DOX showed better efficacy than DOXIL, which may be led by a synergistic effect between the DOX and RA. The R@DOX exhibited slightly better efficacy compared to X-R@DOX due to its fast drug-releasing kinetics (Figure 1h). To investigate the synergistic effect between RA and DOX in Rososome, we calculated the combination index (CI)[48, 49] of the R@DOX and X-R@DOX, parallelly compared with DOXIL and Rososome & X-Rososome. As shown in Figure 2c, the CI of both R@DOX and X-R@DOX stayed lower than 1 at different concentrations, indicating that the RA and DOX can work synergistically in Rososomes, and the rososomal formulation exhibit better efficacy than single model therapy, such as Rososome/X-Rososome and DOXIL. Free DOX and RA are not comparable with R@DOX or X-R@DOX for the synergistic analysis because they didn't experience the drug-releasing process.

3.8. Cell apoptosis by the treatments of Rososomes

Then, we evaluated the cell apoptosis of 4T1 cells by treating them with the same formulations as the cell viability experiments. To avoid killing all the cells, we set the concentration of the treating materials at 5 μM (based on the equivalent concentration of DOX) for apoptosis evaluation. As shown in the flow cytometry results (Figure 2d), free RA, Rososome and X-Rososome only cause slight apoptosis, the percentages of the apoptotic cells (in Q2 area) are 0.62%, 1.10% and 0.75%, respectively. The low apoptosis can be ascribed to the relatively safe concentration of rosmarinic acid. DOXIL contributed more apoptotic cells (3.96% in Q2) due to the high potential of DOX. The free DOX, R@DOX and X-R@DOX induced competitive apoptosis on 4T1 breast cancer cells, which led 5.81%, 9.24% and 8.73% of 4T1 cells become apoptosis, respectively. The apoptotic results were highly consistent with the cell viability results. The better effect of R@DOX and X-R@DOX can be attributed to the synergistic effect between rosmarinic acid and DOX.

3.9. Cell uptake of Rososomes evaluated by flow cytometry

To investigate the cell uptake of Rososomes, we incubated free DOX, DOXIL, R@DOX and X-R@DOX with 4T1 cells and applied to flow cytometry analysis by tracking the intrinsic fluorescence of DOX. The concentrations of these materials were calculated by the equivalent molar concentration of DOX. The PBS-treated cells were set as control. As shown in Figurer 3a, free DOX, R@DOX and X-R@DOX all showed higher cell uptake

compared to the PBS control. Interestingly, DOXIL showed fewer cellular ingestions compared to the other three experimental groups (DOX, R@DOX and X-R@DOX). Although the Rososomes and DOXIL both are liposomes with PEG surface, DOXIL showed lower cell uptake. We speculated that the lower uptake of DOXIL to R@DOX or X-R@DOX may be ascribed to their disparity in surface charge. At in vitro level, the surface charge of the nanoparticle plays a key role in the aspect of cell uptake. Generally, the positively charged nanoparticles tend to absorb on the negatively charged surface of cells by electrostatic interaction, thus promote the cell uptake.[19, 50–52] To investigate the difference between Rososomes and DOXIL, the surface charge of DOXIL was measured (Figure S12). In comparison, the surface charge of DOXIL (−18.1 mV) was much more negative than both R@DOX (−5.86 mV) and X-R@DOX (−2.88 mV). The near-neutral surface charge makes Rososomes are relatively more favorable to the cell uptake than DOXIL.

3.10. Subcellular distributions of Rososomes

The subcellular distributions of the Rososomes were observed by co-localizing the fluorescence of DOX with lysosomes and nucleus (Figure 3b). The Rososomes were indicated by the fluorescence of DOX (green color), LysoTracker Deep Red was employed to stain lysosomes (red color) and the blue color of Hoechst 33342 indicated cell nucleus. In free DOX-treated cells, the green color of DOX largely colocalized with the blue color of the nucleus, indicating that free DOX mostly entered into the nucleus. Also, sporadic green fluorescence distributed outside of the nucleus (blue), and partially colocalized with the lysosomes (red). These co-localization details demonstrated that free DOX can be ingested by cells and accumulated in the cell nucleus and lysosomes. In the DOXIL-treated group, imperceptible green fluorescence co-localized with the blue fluorescence, indicating that less DOXIL entered the nucleus. Part of DOXIL co-localized with lysosomes (red). In the Rososome-treated cells, R@DOX and X-R@DOX both displayed strong green fluorescence in cells and colocalized with nuclear (blue), lysosomes (red). The lysosome retainment indicated that Rososomes may take advantage of the intracellular acidic pH to release the DOX. Comparatively, the crosslinked Rososomes (green) showed relatively low distributions in the nucleus (blue), which was consistent with the drug-releasing pattern in Figure 1h and may explain why the X-R@DOX exhibited less *in vitro* efficacy than R@DOX. The CLSM results are consistent with the flow cytometry data, which demonstrated that the free drug can be readily ingested into cells and enter the cell nucleus, while the liposomal formulations of DOX, including DOXIL, R@DOX and X-R@DOX, showed less nuclear accumulation because they need to go through the drug release process. The cellular uptake and distribution data in Figure 3 can also explain the reason why DOXIL exhibited less efficacy at the in vitro level.

3.11. Pharmacokinetics of Rososomes

The Rososomes were further moved to the *in vivo* evaluations. We claimed that the iron-crosslinking strategy can stabilize the rososomal structure and improve the pharmacokinetics (PK). Therefore, DOX, R@DOX and X-R@DOX were i.v. injected into mice, the DOX concentrations in blood were tested at different timepoints. As shown in Figure 4a and 4b, R@DOX and X-R@DOX both showed a better area under curve (AUC) and circulation time

(T-half) than free DOX. Even the non-crosslinked Rososome showed 5 times longer T-half than free DOX indicating that Rososomes were able to protect the DOX from being prematurely eliminated and improve the PK profile. X-R@DOX showed much higher AUC (629.4) and longer T-half (16.1 h) than R@DOX (AUC is 405.8 and T-half is 6.9 h). The crosslinking strategy can improve the AUC and T-half of Rososomes for more than 1.6 and 2.3 times, respectively. As a commercial liposomal formulation of DOX, the PK of DOXIL has been extensively investigated. Based on the published data[53–56], the T-half of DOXIL is longer than 19 h on mice, which is better than the crosslinked Rososomes. The better PK of DOXIL may be ascribed to its more negative surface charge which can largely reduce the opsonization.[57, 58] Although DOXIL showed better PK, we postulated that Rososome will show better efficacy to DOXIL, due to the synergistic therapeutic effect of doxorubicin and rosmarinic acid.

3.12. Biodistributions of Rososomes

The biodistributions of Rososomes were investigated on subcutaneous 4T1 tumor-bearing mice. The fluorescence of DOX was not accessible to *in vivo* imaging due to the limited penetration. To make Rososomes visible with near-infrared fluorescence, we encapsulated a hydrophilic dye (indocyanine green, ICG) as a drug surrogate and obtained two Rososomes (R@ICG and X-R@ICG). The R@ICG and X-R@ICG were i.v. administrated into 4T1 tumor-bearing mice, respectively. As shown in Figure S12 and Figure 5a, both R@ICG and X-R@ICG accumulated and remained in tumor site for 72 h. To evaluate the biodistribution of Rososomes, the mice were sacrificed, and their tumors and main organs were harvested for *ex vivo* imaging. As shown in Figure 5b, both Rososomes showed the highest accumulation in tumor tissue, indicating that Rososomes preferentially delivered the payloads to tumor site. We also found that livers trapped certain amounts of Rososomes, as nanoparticles intend to accumulate in the reticuloendothelial system.[58–60] Comparatively, the accumulation of X-Rososome in tumor was significantly higher than Rososome (Figure 5c), which further supported the advantages of our crosslinking strategy.

3.13. In vivo anti-tumor efficacy of Rososomes on orthotopic breast cancer

The Rososomes were applied to tumor-bearing mice to evaluate the synergistic anti-cancer efficacy *in vivo*. 4T1 tumor-bearing mice were randomly distributed into 7 cohorts (n=6), including the groups treated with PBS, free DOX, DOXIL, Rososome, X-Rososome, R@DOX and X-R@DOX. The mice were i.v. injected with these materials every three days for two consecutive weeks. The dose of the formulations was calculated corresponding to the equivalent concentration of DOX (8 mg/kg). As shown in Figure 5d, 4T1 breast cancer is highly aggressive, free DOX only showed slight efficacy. In comparison, both empty Rososomes exhibited better efficacy than free DOX on slowing down the tumor progression, demonstrating the ROS-therapy also contributed some extent of anti-cancer efficacy. The R@DOX exhibited an effective tumor-suppression effect which is similar to DOXIL. The X-R@DOX showed the best anti-cancer efficacy which can effectively suppress tumor growth. The efficacy of X-R@DOX was significantly better than other groups, including the DOXIL and R@DOX, which can be attributed to the synergistic efficacy of RA and DOX, and the better PK contributed by our crosslinking strategy. The *in vivo* anti-cancer effect

demonstrated that our iron crosslinked Rososomes showed great potential for synergistic cancer therapy.

3.14. Biocompatibility of Rososomes

The bodyweight of mice didn't show obvious changes during the treatment, indicating good biocompatibility of Rososomes (Figure 5e). To study the systemic toxicity, X-R@DOX treated mice were sacrificed, and the organs were collected for hematoxylin and eosin (H&E) stain. As shown in Figure 5f, the main organs, including heart, liver, spleen, lung and kidney, didn't show any abnormality, indicating that the doxorubicin encapsulated, crosslinked Rososome is safe for biological use.

4. Conclusions

In this work, we developed a novel crosslinking strategy for the construction of liposomes with robust stability, high drug loading and synergistic anti-cancer efficacy. We encapsulated 25.8% ROS producer (RA) and 9.04% chemotherapeutic drug (DOX) in the newly developed Rososome, in which RA can effectively level up the oxidative stress in cells and work synergistically with DOX. The crosslinking strategy can extensively stabilize the liposomal structure of Rososomes and improve the pharmacokinetic profile. The synergistic efficacy and better pharmacokinetics led to better anti-cancer efficacy on the syngeneic breast cancer mouse model, comparing to the corresponding single model therapy and a commercial liposomal formulation of DOX (DOXIL). This work provides a valuable crosslinking strategy to develop robust liposomal formulation with robust stability, high drug loading and synergistic anti-cancer efficacy.

Supplementary Material

Refer to Web version on PubMed Central for supplementary material.

Acknowledgments

We thank the financial support from NIH/NCI (R01CA199668, R01CA232845), NIH/NIDCR (R01DE029237), NIH/NICHD (R01HD086195), and UC Davis Comprehensive Cancer Center Support Grant (CCSG) awarded by the National Cancer Institute (NCI P30CA093373).

References

[1]. Moore HC, Unger JM, Phillips K-A, Boyle F, Hitre E, Porter D, Francis PA, Goldstein LJ, Gomez HL, Vallejos CS, Goserelin for ovarian protection during breast-cancer adjuvant chemotherapy, N. Engl. J. Med 372(10) (2015) 923–932. [PubMed: 25738668]

[2]. Romond EH, Perez EA, Bryant J, Suman VJ, Geyer CE Jr, Davidson NE, Tan-Chiu E, Martino S, Paik S, Kaufman PA, Trastuzumab plus adjuvant chemotherapy for operable HER2-positive n breast cancer, N. Engl. J. Med 353(16) (2005) 1673–1684. [PubMed: 16236738]

[3]. Love RR, Leventhal H, Easterling DV, Nerenz DR, Side effects and emotional distress during cancer chemotherapy, Cancer 63(3) (1989) 604–612. [PubMed: 2912536]

[4]. Carelle N, Piotto E, Bellanger A, Germanaud J, Thuillier A, Khayat D, Changing patient perceptions of the side effects of cancer chemotherapy, Cancer 95(1) (2002) 155–163. [PubMed: 12115329]

[5]. Zhang W, Guo Z, Huang D, Liu Z, Guo X, Zhong H, Synergistic effect of chemo-photothermal therapy using PEGylated graphene oxide, Biomaterials 32(33) (2011) 8555–8561. [PubMed: 21839507]

[6]. Wei W, Lv P-P, Chen X-M, Yue Z-G, Fu Q, Liu S-Y, Yue H, Ma G-H, Codelivery of mTERT siRNA and paclitaxel by chitosan-based nanoparticles promoted synergistic tumor suppression, Biomaterials 34(15) (2013) 3912–3923. [PubMed: 23453062]

[7]. Mi Y, Liu X, Zhao J, Ding J, Feng S-S, Multimodality treatment of cancer with herceptin conjugated, thermomagnetic iron oxides and docetaxel loaded nanoparticles of biodegradable polymers, Biomaterials 33(30) (2012) 7519–7529. [PubMed: 22809649]

[8]. Chen H, Zhang W, Zhu G, Xie J, Chen X, Rethinking cancer nanotheranostics, Nat. Rev. Mater 2(7) (2017) 17024. [PubMed: 29075517]

[9]. Lu Y, Aimetti AA, Langer R, Gu Z, Bioresponsive materials, Nat. Rev. Mater 1 (2016) 16075.

[10]. Xue X, Lindstrom A, Qu H, Li Y, Recent advances on small-molecule nanomedicines for cancer treatment, WIREs Nanomed. Nanobiotech. 12(3) (2019) e1607.

[11]. Xue X, Zhao Y, Dai L, Zhang X, Hao X, Zhang C, Huo S, Liu J, Liu C, Kumar A, Chen W-Q, Zou G, Liang X-J, Spatiotemporal Drug Release Visualized through a Drug Delivery System with Tunable Aggregation-Induced Emission, Adv. Mater 26(5) (2014) 712–717. [PubMed: 24129910]

[12]. Iyer AK, Khaled G, Fang J, Maeda H, Exploiting the enhanced permeability and retention effect for tumor targeting, Drug Discover. Today 11(17) (2006) 812–818.

[13]. Sindhwani S, Syed AM, Ngai J, Kingston BR, Maiorino L, Rothschild J, MacMillan P, Zhang Y, Rajesh NU, Hoang T, Wu JLY, Wilhelm S, Zilman A, Gadde S, Sulaiman A, Ouyang B, Lin Z, Wang L, Egeblad M, Chan WCW, The entry of nanoparticles into solid tumours, Nat. Mater 19(5) (2020) 566–575. [PubMed: 31932672]

[14]. Matés JM, Sánchez-Jiménez FM, Role of reactive oxygen species in apoptosis: implications for cancer therapy, Int. J. Biochem. Cell Biol 32(2) (2000) 157–170. [PubMed: 10687951]

[15]. Zhou Z, Song J, Nie L, Chen X, Reactive oxygen species generating systems meeting challenges of photodynamic cancer therapy, Chem. Soc. Rev 45(23) (2016) 6597–6626. [PubMed: 27722328]

[16]. Tong L, Chuang C-C, Wu S, Zuo L, Reactive oxygen species in redox cancer therapy, Cancer Lett. 367(1) (2015) 18–25. [PubMed: 26187782]

[17]. Dai Y, Yang Z, Cheng S, Wang Z, Zhang R, Zhu G, Wang Z, Yung BC, Tian R, Jacobson O, Xu C, Ni Q, Song J, Sun X, Niu G, Chen X, Toxic Reactive Oxygen Species Enhanced Synergistic Combination Therapy by Self-Assembled Metal-Phenolic Network Nanoparticles, Adv. Mater 30(8) (2018)1704877.

[18]. Xue X, Huang Y, Wang X, Wang Z, Carney RP, Li X, Yuan Y, He Y, Lin T.-y., Li Y, Self-indicating, fully active pharmaceutical ingredients nanoparticles (FAPIN) for multimodal imaging guided trimodality cancer therapy, Biomaterials 161 (2018) 203–215. [PubMed: 29421556]

[19]. Xue X, Huang Y, Bo R, Jia B, Wu H, Yuan Y, Wang Z, Ma Z, Jing D, Xu X, Yu W, Lin T.-y., Li Y, Trojan Horse nanotheranostics with dual transformability and multifunctionality for highly effective cancer treatment, Nat. Commun 9(1) (2018) 3653. [PubMed: 30194413]

[20]. Xiao Y-F, Chen J-X, Li S, Tao W-W, Tian S, Wang K, Cui X, Huang Z, Zhang X-H, Lee C-S, Manipulating exciton dynamics of thermally activated delayed fluorescence materials for tuning two-photon nanotheranostics, Chem. Sci 11(3) (2020) 888–895.

[21]. Chen H, Li S, Wu M, Kenry Huang Z, Lee C-S, Liu B, Membrane-Anchoring Photosensitizer with Aggregation-Induced Emission Characteristics for Combating Multidrug-Resistant Bacteria, Angew. Chem. Int. Ed 59(2) (2020) 632–636.

[22]. Zhang J, Fang F, Liu B, Tan J-H, Chen W-C, Zhu Z, Yuan Y, Wan Y, Cui X, Li S, Tong Q-X, Zhao J, Meng X-M, Lee C-S, Intrinsically Cancer-Mitochondria-Targeted Thermally Activated Delayed Fluorescence Nanoparticles for Two-Photon-Activated Fluorescence Imaging and Photodynamic Therapy, ACS Appl. Mater. Interfaces 11(44) (2019) 41051–41061. [PubMed: 31602976]

[23]. Xue X, Lindstrom A, Li Y, Porphyrin-Based Nanomedicines for Cancer Treatment, Bioconj. Chem 30(6) (2019)1585–1603.

[24]. Zou Z, Chang H, Li H, Wang S, Induction of reactive oxygen species: an emerging approach for cancer therapy, Apoptosis 22(11) (2017) 1321–1335. [PubMed: 28936716]

[25]. Lecumberri E, Dupertuis YM, Miralbell R, Pichard C, Green tea polyphenol epigallocatechin-3-gallate (EGCG) as adjuvant in cancer therapy, Clin. Nutr 32(6) (2013) 894–903. [PubMed: 23582951]

[26]. Jin H-O, Yoon S-I, Seo S-K, Lee H-C, Woo S-H, Yoo D-H, Lee S-J, Choe T-B, An S, Kwon T-J, Kim J-I, Park M-J, Hong S-I, Park I-C, Rhee C-H, Synergistic induction of apoptosis by sulindac and arsenic trioxide in human lung cancer A549 cells via reactive oxygen species-dependent down-regulation of survivin, Biochem. Pharmacol 72(10) (2006) 1228–1236. [PubMed: 16950207]

[27]. Li X, Zhu F, Jiang J, Sun C, Wang X, Shen M, Tian R, Shi C, Xu M, Peng F, Guo X, Wang M, Qin R, Synergistic antitumor activity of withaferin A combined with oxaliplatin triggers reactive oxygen species-mediated inactivation of the PI3K/AKT pathway in human pancreatic cancer cells, Cancer Lett. 357(1) (2015) 219–230. [PubMed: 25444914]

[28]. Yu C, Friday BB, Lai J-P, McCollum A, Atadja P, Roberts LR, Adjei AA, Abrogation of MAPK and Akt Signaling by AEE788 Synergistically Potentiates Histone Deacetylase Inhibitor-Induced Apoptosis through Reactive Oxygen Species Generation, Clin. Cancer Res 13(4) (2007) 1140–1148. [PubMed: 17317822]

[29]. Zhuang X, Ma X, Xue X, Jiang Q, Song L, Dai L, Zhang C, Jin S, Yang K, Ding B, Wang PC, Liang X-J, A Photosensitizer-Loaded DNA Origami Nanosystem for Photodynamic Therapy, ACS Nano 10(3) (2016) 3486–3495. [PubMed: 26950644]

[30]. Xu J, Xu L, Wang C, Yang R, Zhuang Q, Han X, Dong Z, Zhu W, Peng R, Liu Z, Near-Infrared-Triggered Photodynamic Therapy with Multitasking Upconversion Nanoparticles in Combination with Checkpoint Blockade for Immunotherapy of Colorectal Cancer, ACS Nano 11(5) (2017) 4463–4474. [PubMed: 28362496]

[31]. Gong N, Ma X, Ye X, Zhou Q, Chen X, Tan X, Yao S, Huo S, Zhang T, Chen S, Teng X, Hu X, Yu J, Gan Y, Jiang H, Li J, Liang X-J, Carbon-dot-supported atomically dispersed gold as a mitochondrial oxidative stress amplifier for cancer treatment, Nat. Nanotechnol 14(4) (2019) 379–387. [PubMed: 30778211]

[32]. Trachootham D, Alexandre J, Huang P, Targeting cancer cells by ROS-mediated mechanisms: a radical therapeutic approach?, Nat. Rev. Drug Discover 8(7) (2009) 579–591.

[33]. Li Y, Xiao K, Luo J, Xiao W, Lee JS, Gonik AM, Kato J, Dong TA, Lam KS, Well-defined, reversible disulfide cross-linked micelles for on-demand paclitaxel delivery, Biomaterials 32(27) (2011) 6633–6645. [PubMed: 21658763]

[34]. Zhu C, Jung S, Luo S, Meng F, Zhu X, Park TG, Zhong Z, Co-delivery of siRNA and paclitaxel into cancer cells by biodegradable cationic micelles based on PDMAEMA–PCL–PDMAEMA triblock copolymers, Biomaterials 31(8) (2010) 2408–2416. [PubMed: 19963269]

[35]. Zhang CY, Yang YQ, Huang TX, Zhao B, Guo XD, Wang JF, Zhang LJ, Self-assembled pH-responsive MPEG-b-(PLA-co-PAE) block copolymer micelles for anticancer drug delivery, Biomaterials 33(26) (2012) 6273–6283. [PubMed: 22695069]

[36]. Petersen M, Simmonds MSJ, Rosmarinic acid, Phytochemistry 62(2) (2003) 121–125. [PubMed: 12482446]

[37]. Petersen M, Abdullah Y, Benner J, Eberle D, Gehlen K, Hücherig S, Janiak V, Kim KH, Sander M, Weitzel C, Wolters S, Evolution of rosmarinic acid biosynthesis, Phytochemistry 70(15) (2009) 1663–1679. [PubMed: 19560175]

[38]. Araniti F, Costas-Gil A, Cabeiras-Freijanes L, Lupini A, Sunseri F, Reigosa MJ, Abenavoli MR, Sánchez-Moreiras AM, Rosmarinic acid induces programmed cell death in Arabidopsis seedlings through reactive oxygen species and mitochondrial dysfunction, PLOS ONE 13(12) (2018) e0208802. [PubMed: 30586368]

[39]. Murakami K, Haneda M, Qiao S, Naruse M, Yoshino M, Prooxidant action of rosmarinic acid: Transition metal-dependent generation of reactive oxygen species, Toxicol. in Vitro 21(4) (2007) 613–617. [PubMed: 17267171]

[40]. Sedó J, Saiz-Poseu J, Busqué F, Ruiz-Molina D, Catechol-Based Biomimetic Functional Materials, Adv. Mater 25(5) (2013) 653–701. [PubMed: 23180685]

[41]. Kawabata T, Schepkin V, Haramaki N, Phadke RS, Packer L, Iron coordination by catechol derivative antioxidants, Biochem. Pharmacol 51(11) (1996) 1569–1577. [PubMed: 8630099]

[42]. Azevedo S, Costa AMS, Andersen A, Choi IS, Birkedal H, Mano JF, Bioinspired Ultratough Hydrogel with Fast Recovery, Self-Healing, Injectability and Cytocompatibility, Adv. Mater 29(28) (2017) 1700759.

[43]. Xue X, Bo R, Qu H, Jia B, Xiao W, Yuan Y, Vapniarsky N, Lindstrom A, Wu H, Zhang D, Li L, Ricci M, Ma Z, Zhu Z, Lin T.-y., Louie AY, Li Y, A nephrotoxicity-free, iron-based contrast agent for magnetic resonance imaging of tumors, Biomaterials 257 (2020) 120234. [PubMed: 32736259]

[44]. Li S, Zou Q, Li Y, Yuan C, Xing R, Yan X, Smart Peptide-Based Supramolecular Photodynamic Metallo-Nanodrugs Designed by Multicomponent Coordination Self-Assembly, J. Am. Chem. Soc 140(34) (2018) 10794–10802. [PubMed: 30102029]

[45]. Giliopoulos D, Zamboulis A, Giannakoudakis D, Bikiaris D, Triantafyllidis K, Polymer/Metal Organic Framework (MOF) Nanocomposites for Biomedical Applications, Molecules 25(1) (2020) 185.

[46]. Tang L, Shi J, Wang X, Zhang S, Wu H, Sun H, Jiang Z, Coordination polymer nanocapsules prepared using metal-organic framework templates for pH-responsive drug delivery, Nanotechnology 28(27) (2017) 275601. [PubMed: 28510533]

[47]. Xue X, Jin S, Zhang C, Yang K, Huo S, Chen F, Zou G, Liang X-J, Probe-Inspired NanoProdrug with Dual-Color Fluorogenic Property Reveals Spatiotemporal Drug Release in Living Cells, ACS Nano 9(3) (2015) 2729–2739. [PubMed: 25688453]

[48]. Chou T-C, Drug Combination Studies and Their Synergy Quantification Using the Chou-Talalay Method, Cancer Res. 70(2) (2010) 440–446. [PubMed: 20068163]

[49]. Chou T-C, Theoretical Basis, Experimental Design, and Computerized Simulation of Synergism and Antagonism in Drug Combination Studies, Pharmacol. Rev 58(3) (2006) 621–681. [PubMed: 16968952]

[50]. Du J-Z, Sun T-M, Song W-J, Wu J, Wang J, A Tumor-Acidity-Activated Charge-Conversional Nanogel as an Intelligent Vehicle for Promoted Tumoral-Cell Uptake and Drug Delivery, Angew. Chem. Int. Ed 49(21) (2010) 3621–3626.

[51]. Sun C-Y, Shen S, Xu C-F, Li H-J, Liu Y, Cao Z-T, Yang X-Z, Xia J-X, Wang J, Tumor Acidity-Sensitive Polymeric Vector for Active Targeted siRNA Delivery, J. Am. Chem. Soc 137(48) (2015) 15217–15224. [PubMed: 26571079]

[52]. Guan X, Guo Z, Lin L, Chen J, Tian H, Chen X, Ultrasensitive pH Triggered Charge/Size Dual-Rebound Gene Delivery System, Nano Lett. 16(11) (2016) 6823–6831. [PubMed: 27643629]

[53]. Mamidi RNVS, Weng S, Stellar S, Wang C, Yu N, Huang T, Tonelli AP, Kelley MF, Angiuoli A, Fung M-C, Pharmacokinetics, efficacy and toxicity of different pegylated liposomal doxorubicin formulations in preclinical models: is a conventional bioequivalence approach sufficient to ensure therapeutic equivalence of pegylated liposomal doxorubicin products?, Cancer Chemother. Pharmacol 66(6) (2010) 1173–1184. [PubMed: 20661737]

[54]. Smith JA, Mathew L, Burney M, Nyshadham P, Coleman RL, Equivalency challenge: Evaluation of Lipodox® as the generic equivalent for Doxil® in a human ovarian cancer orthotropic mouse model, Gynecol. Oncol 141(2) (2016) 357–363. [PubMed: 26946092]

[55]. Gabizon A, Tzemach D, Mak L, Bronstein M, Horowitz AT, Dose Dependency of Pharmacokinetics and Therapeutic Efficacy of Pegylated Liposomal Doxorubicin (DOXIL) in Murine Models, J. Drug Target 10(7) (2002) 539–548. [PubMed: 12683721]

[56]. Working PK, Newman MS, Huang SK, Mayhew E, Vaage J, Lasic DD, Pharmacokinetics, Biodistribution and Therapeutic Efficacy of Doxorubicin Encapsulated in Stealth® Liposomes (Doxil®), J. Liposome Res 4(1) (1994) 667–687.

[57]. Owens DE, Peppas NA, Opsonization, biodistribution, and pharmacokinetics of polymeric nanoparticles, Int. J. Pharm 307(1) (2006) 93–102. [PubMed: 16303268]

[58]. Moghimi SM, Szebeni J, Stealth liposomes and long circulating nanoparticles: critical issues in pharmacokinetics, opsonization and protein-binding properties, Prog. Lipid Res 42(6) (2003) 463–478. [PubMed: 14559067]

[59]. Hirn S, Semmler-Behnke M, Schleh C, Wenk A, Lipka J, Schäffler M, Takenaka S, Möller W, Schmid G, Simon U, Kreyling WG, Particle size-dependent and surface charge-dependent biodistribution of gold nanoparticles after intravenous administration, Eur. J. Pharm. Biopharm 77(3) (2011) 407–416. [PubMed: 21195759]

[60]. Li S-D, Huang L, Stealth nanoparticles: High density but sheddable PEG is a key for tumor targeting, J. Control. Release 145(3) (2010) 178–181. [PubMed: 20338200]

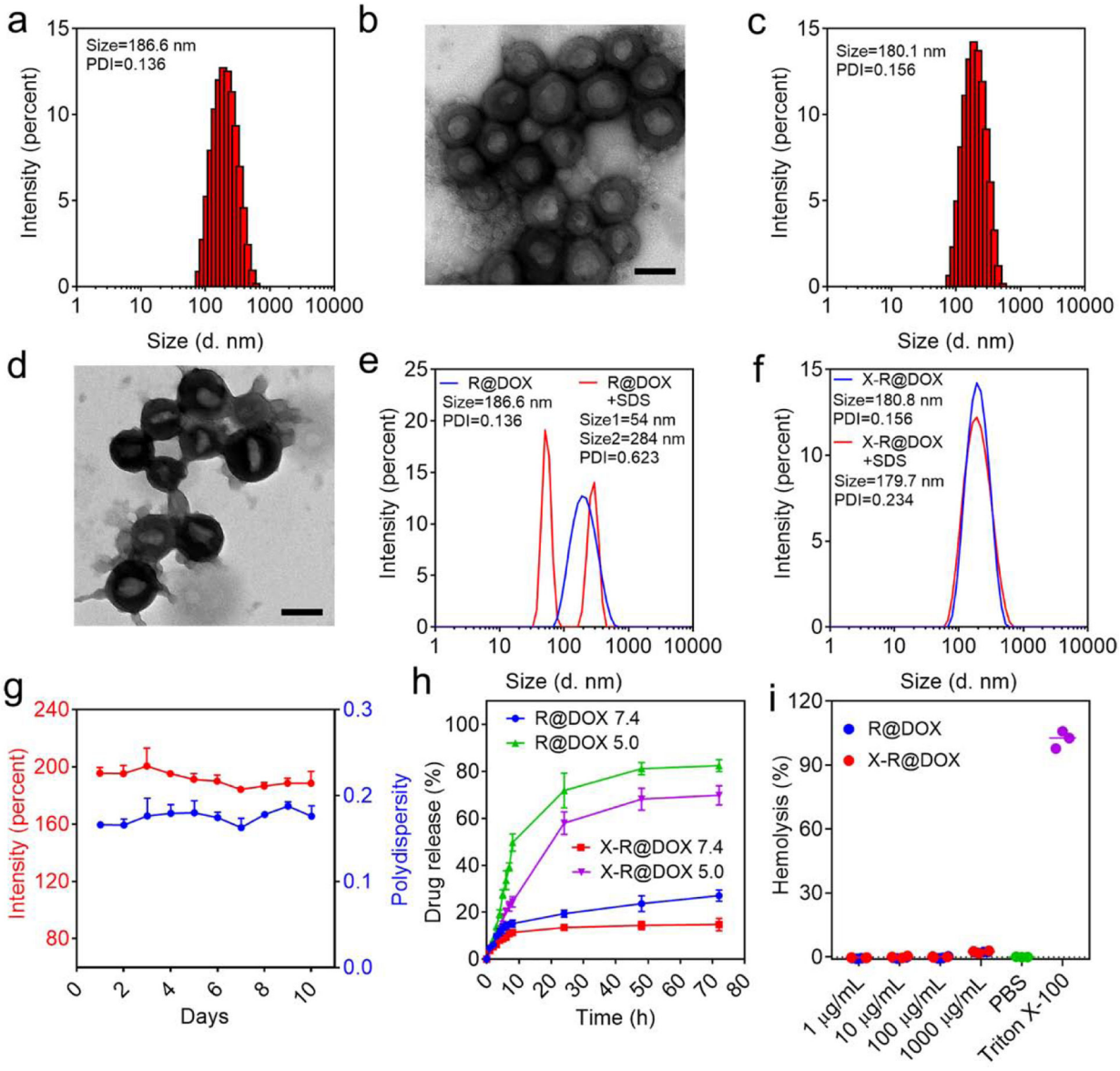

Figure 1. Characterization of Rososomes.

a) The size distribution of R@DOX measured by DLS. b) The morphology of R@DOX observed by TEM. The scale bar is 100 nm. c) The size distribution of X-R@DOX measured by DLS. d) The morphology of X-R@DOX observed by TEM. The scale bar is 100 nm. Stability investigation of e) R@DOX and f) X-R@DOX to prove the benefits of iron-catechol crosslinking strategy. The Rososomes were incubated with 2 mM SDS for 12 h, the changes in size and PDI were monitored by DLS. g) Serum stability of X-R@DOX monitored by DLS. The size increases of R@DOX and X-R@DOX at Day 1 were attributed to the protein binding and the formation of protein corona, as the Rososomes were incubated with fetal bovine serum for the stability tests. h) Accumulative drug release of R@DOX and X-R@DOX by the stimulation of acidic pH (5.0). i) Hemolysis of Rososomes. PBS and Triton X-100 were employed as negative and positive control, respectively.

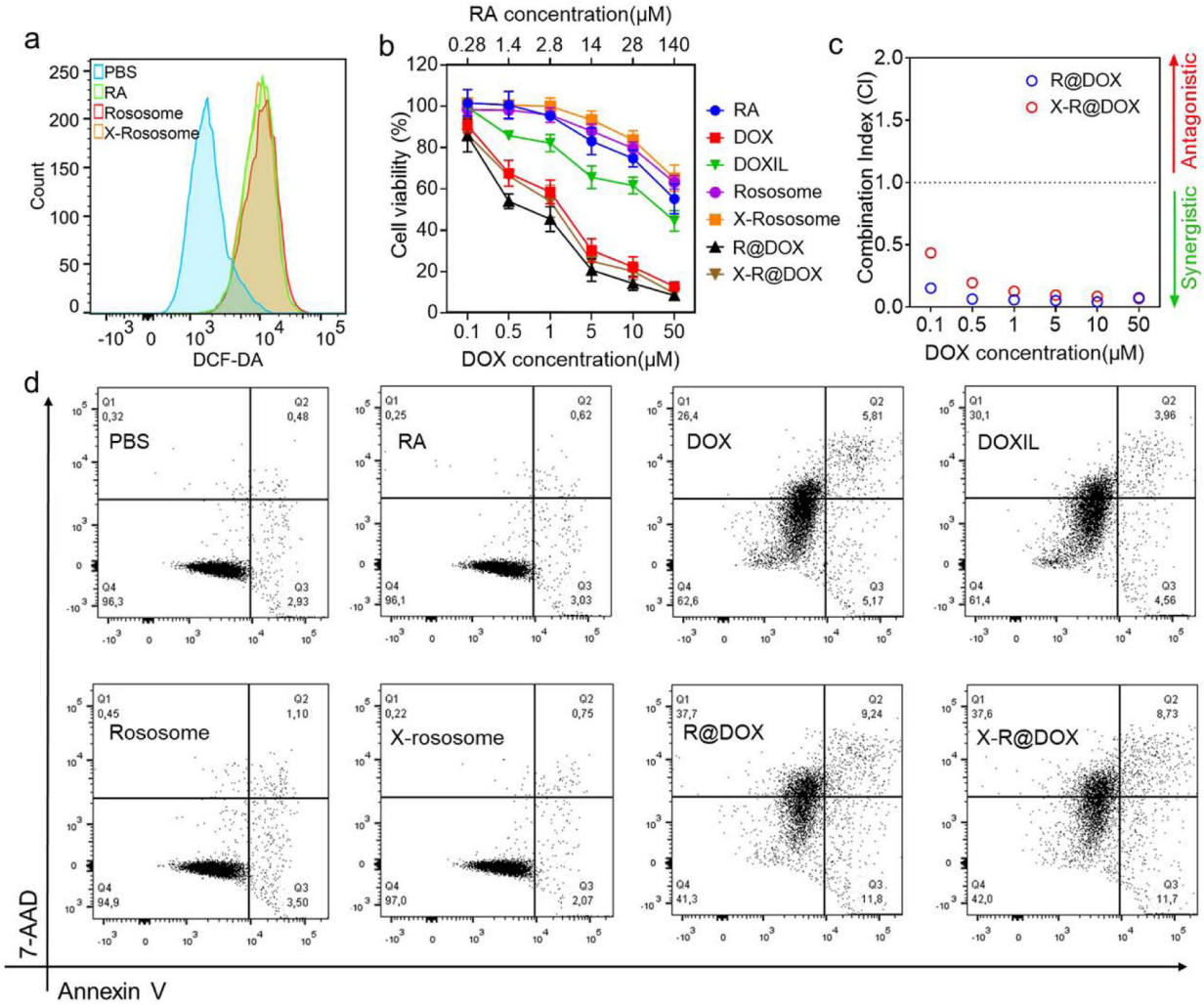

Figure 2. ***In vitro*** **anticancer efficiency of Rososomes on 4T1 breast cancer cells.**

a) The ROS production at the cellular level. 4T1 cells were treated with RA, Rososome and X-Rososome for 12 h and stained with a ROS probe (DCF-DA) for flow cytometry analysis. b) Cell viability of 4T1 cells that treated with different materials. c) The combination index of RA and DOX in R@DOX and X-R@DOX. The plot of CI versus drug concentrations was generated by CompuSyn software, based on the cell viability results. d) Cell apoptosis evaluation of Rososomes and their controls. The 4T1 cells were incubated with different materials for 24 h and stained by Annexin V and 7-Aminoactinomycin D (7-AAD) for flow cytometry analysis. The concentrations of these materials were calculated by the equivalent molar concentration of DOX (5 μM).

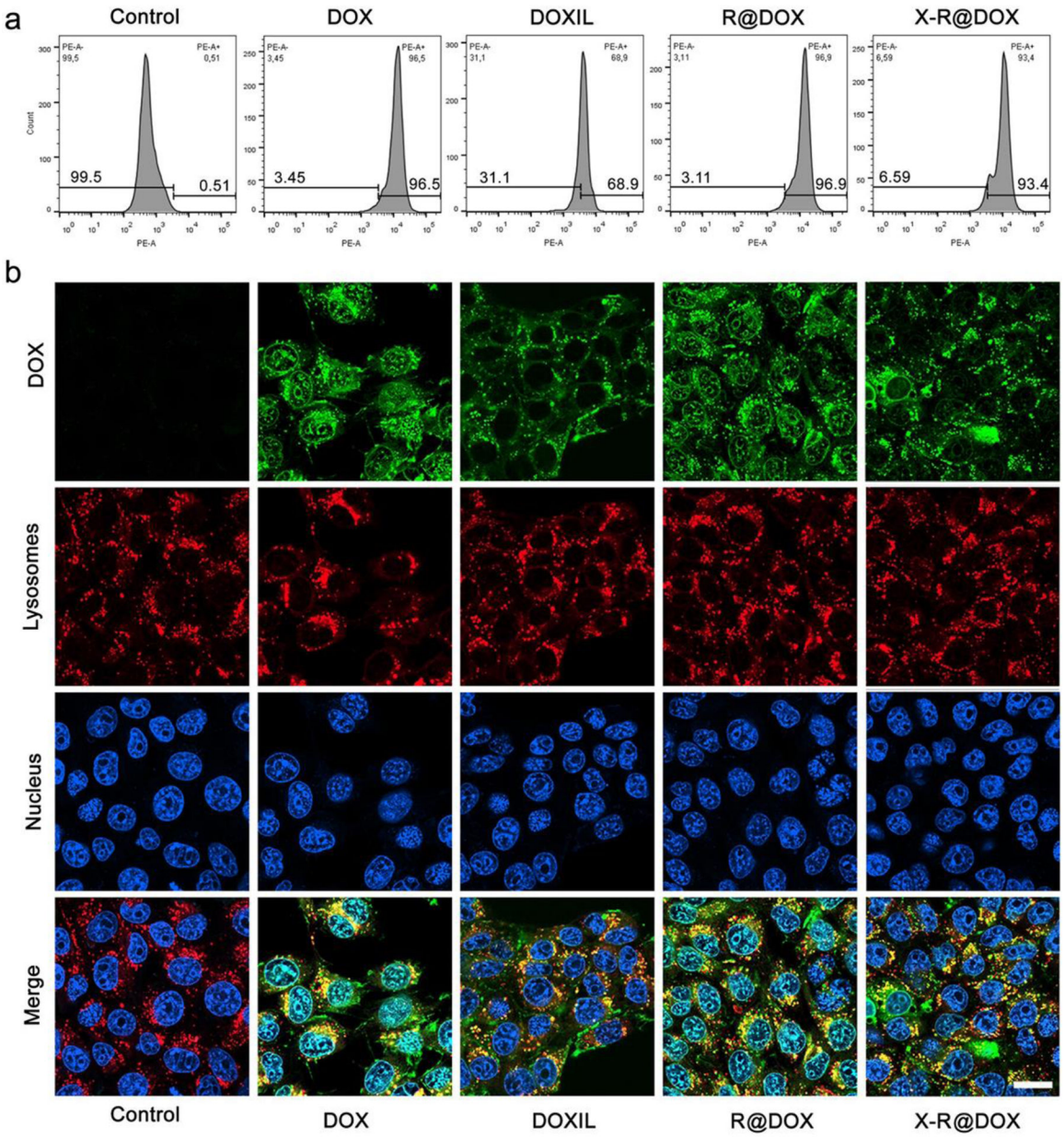

Figure 3. Cell uptake and intracellular distributions of Rososomes in 4T1 breast cancer cells.

a) The quantitative cellular uptake of DOX, DOXIL, R@DOX and X-R@DOX measured by flow cytometry. b) Subcellular distributions of DOX, DOXIL, R@DOX and X-R@DOX on 4T1 breast cancer cells. LysoTracker Deep Red is employed to stain lysosomes and Hoechst 33342 is for the nucleus. The scale bar is 20 μm. The doses were calculated based on the equivalent molar concentration of DOX.

a

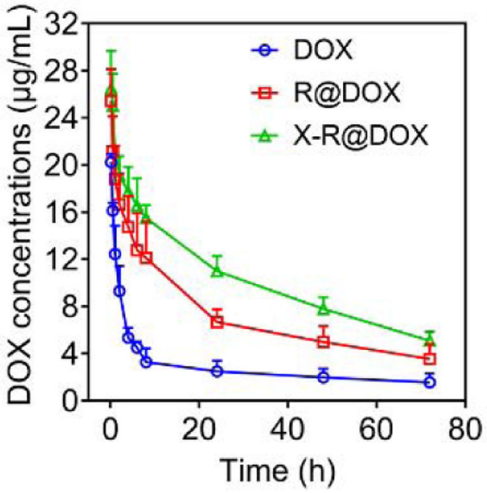

b

Materials	AUC	T-half (h)
DOX	92.27	1.38
R@DOX	405.8	6.9
X-R@DOX	629.4	16.1

Figure 4.

Pharmacokinetics of Rososomes. a) Pharmacokinetics of free DOX, R@DOX and X-R@DOX on mice (n=3). b) The area under curve (AUC) and T-half of free DOX, R@DOX and X-R@DOX, calculated by Kinetica 5.0. The treating doses were calculated based on the equivalent molar concentration of DOX.

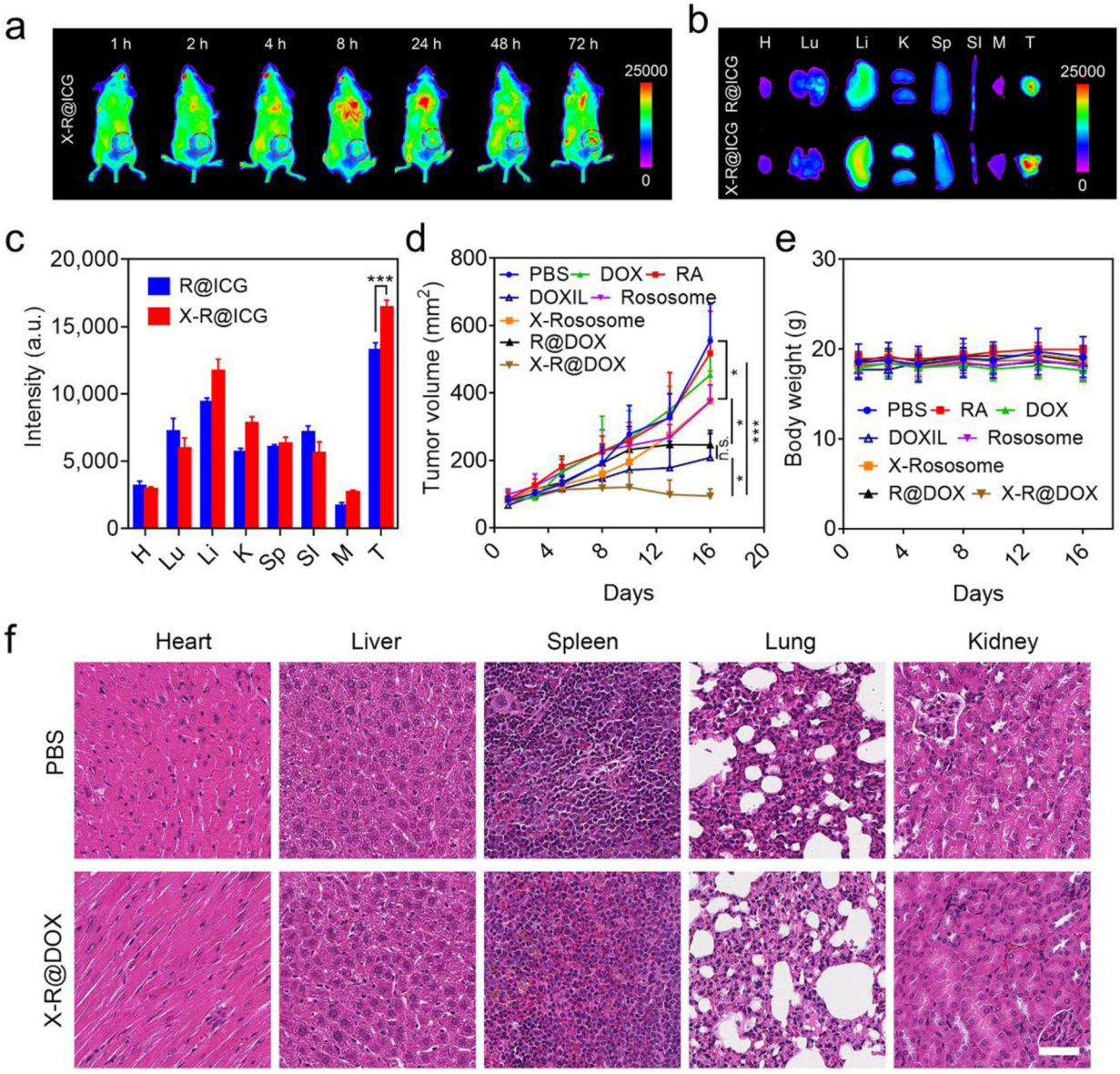

Figure 5. ***In vivo*** **performance of Rososomes on orthotopic 4T1 breast cancer-bearing mice.**

a) *In vivo* near-infrared fluorescence imaging of X-R@ICG treated 4T1 tumor-bearing mice. The red circles point out tumor locations. The high signal on the chest is the reflection from fur. b) *Ex vivo* distribution of R@ICG and X-R@ICG. H, heart; Lu, lung; Li, liver; K, kidney; Sp, spleen; SI, small intestine; M, muscle; T, tumor. c) Quantitative analysis of the biodistributions of Rososomes (n=3) based on b). The concentration of R@ICG and X-R@ICG are calculated based on the equivalent concentration of ICG. d) *In vivo* anti-cancer efficiency of Rososomes on orthotopic 4T1 tumor-bearing mice. f) Bodyweight changes of the mice treated with Rososomes and their controls. f) H&E stain evaluation of systemic toxicity of X-R@DOX. Scale bar is 50 μm. *n.s.* not significantly; *, $p<0.05$; **, $p<0.01$; ***, $p<0.001$.

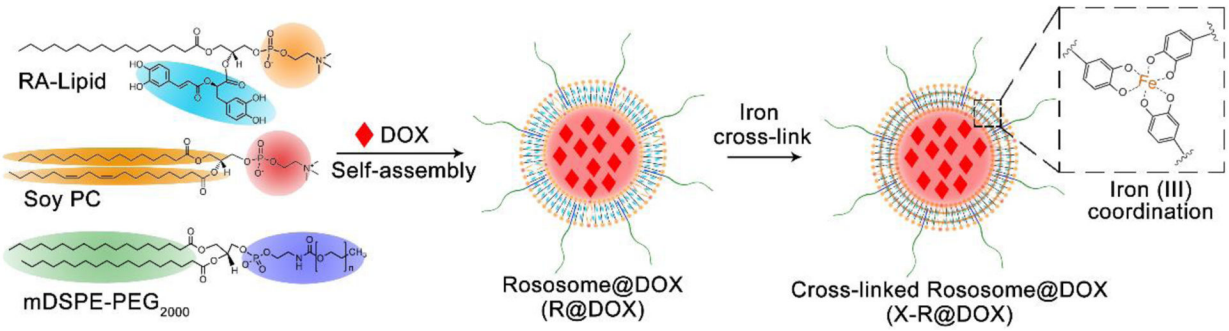

Scheme 1.

Self-assembly of iron cross-linked Rososome encapsulated doxorubicin (X-R@DOX).